Geophysical Journal International

Geophys. J. Int. (2019) **219,** S152–S166
doi: 10.1093/gji/ggz312
Advance Access publication 2019 July 11
GJI Seismology

An investigation of seismic anisotropy in the lowermost mantle beneath Iceland

Jonathan Wolf,[1,2] Neala Creasy,[2] Angelo Pisconti,[1] Maureen D. Long[2] and Christine Thomas[1]

[1]*Institut für Geophysik, University of Münster, Corrensstrasse 24, 48149 Münster, Germany. E-mail: jonathan.wolf@yale.edu*
[2]*Department of Geology and Geophysics, Yale University, New Haven, CT, USA*

Accepted 2019 July 6. Received 2019 June 20; in original form 2018 December 14

SUMMARY

Iceland represents one of the most well-known examples of hotspot volcanism, but the details of how surface volcanism connects to geodynamic processes in the deep mantle remain poorly understood. Recent work has identified evidence for an ultra-low velocity zone in the lowermost mantle beneath Iceland and argued for a cylindrically symmetric upwelling at the base of a deep mantle plume. This scenario makes a specific prediction about flow and deformation in the lowermost mantle, which can potentially be tested with observations of seismic anisotropy. Here we present an investigation of seismic anisotropy in the lowermost mantle beneath Iceland, using differential shear wave splitting measurements of S–ScS and SKS–SKKS phases. We apply our techniques to waves propagating at multiple azimuths, with the goal of gaining good geographical and azimuthal coverage of the region. Practical limitations imposed by the suboptimal distribution of global seismicity at the relevant distance ranges resulted in a relatively small data set, particularly for S–ScS. Despite this, however, our measurements of ScS splitting due to lowermost mantle anisotropy clearly show a rotation of the fast splitting direction from nearly horizontal for two sets of paths that sample away from the low velocity region (implying $V_{SH} > V_{SV}$) to nearly vertical for a set of paths that sample directly beneath Iceland (implying $V_{SV} > V_{SH}$). We also find evidence for sporadic SKS–SKKS discrepancies beneath our study region; while the geographic distribution of discrepant pairs is scattered, those pairs that sample closest to the base of the Iceland plume tend to be discrepant. Our measurements do not uniquely constrain the pattern of mantle flow. However, we carried out simple ray-theoretical forward modelling for a suite of plausible anisotropy mechanisms, including those based on single-crystal elastic tensors, those obtained via effective medium modelling for partial melt scenarios, and those derived from global or regional models of flow and texture development in the deep mantle. These simplified models do not take into account details such as possible transitions in anisotropy mechanism or deformation regime, and test a simplified flow field (vertical flow beneath the plume and horizontal flow outside it) rather than more detailed flow scenarios. Nevertheless, our modelling results demonstrate that our ScS splitting observations are generally consistent with a flow scenario that invokes nearly vertical flow directly beneath the Iceland hotspot, with horizontal flow just outside this region.

Key words: Seismic anisotropy; Composition and structure of the mantle; Atlantic Ocean; Phase transitions.

1 INTRODUCTION

The Iceland landmass is the result of particularly vigorous mantle melting and volcanic activity along the Mid-Atlantic Ridge. It is often discussed as the juxtaposition of a deep mantle plume and a mid-ocean spreading centre (e.g. Gudmundsson 2000), but other models that do not invoke a mantle plume have also been proposed (e.g. Foulger & Anderson 2005). The interpretation of mantle tomography models beneath Iceland and the depth extent of low-velocity anomalies have been particularly controversial (e.g. Wolfe *et al.* 1997). Recent seismic imaging results have argued for a broad, deeply rooted low velocity anomaly extending to the base of the mantle beneath Iceland (French & Romanowicz 2015). There is also observational evidence for the presence of an ultra-low velocity zone (ULVZ) just above the core–mantle boundary (CMB) beneath Iceland (Yuan & Romanowicz 2017; for a summary of ULVZ locations see Yu & Garnero 2018), possibly indicating partial melting (Yuan & Romanowicz 2017). Despite recent progress on imaging the mantle, however, the nature of the connection between Icelandic volcanism and deep mantle processes remains imperfectly understood. One potential avenue for progress involves direct observational constraints on the existence and nature of seismic anisotropy in the lowermost mantle beneath Iceland, which have the potential to illuminate patterns of flow and deformation just above the CMB. Specifically, if observations of anisotropy can provide evidence for a contrast in anisotropy between the lowermost mantle directly beneath Iceland (i.e. at the root of the putative Iceland plume) and the surrounding mantle, this could provide (indirect) evidence for a local perturbation to the generally horizontal flow field expected to dominate the mantle's bottom boundary layer.

Seismic anisotropy, the directional dependence of seismic wave propagation speeds, is commonly used to study mantle flow and deformation (e.g. Long & Becker 2010; Nowacki *et al.* 2010). Observational studies of anisotropy commonly target the upper mantle; however, anisotropy is also present in the mantle transition zone (e.g. Foley & Long 2011), the uppermost lower mantle (e.g. Foley & Long 2011), and the D$''$ layer (the lowermost 300 km of the mantle; (e.g. Wookey *et al.* 2005a; Nowacki *et al.* 2011; Lynner & Long 2014; Creasy *et al.* 2017; Deng *et al.* 2017). In contrast, the bulk of the lower mantle appears to be (nearly) isotropic (e.g. Panning & Romanowicz 2006). Constraints on seismic anisotropy can potentially facilitate the understanding of the mineralogy and temperature conditions, presence and distribution of partial melt, and geometry of flow in the lower mantle (e.g. Long & Silver 2009; Long & Becker 2010; Nowacki *et al.* 2011). Seismic anisotropy can be caused by crystallographic or lattice preferred orientation (CPO or LPO) of anisotropic minerals (e.g. Karato *et al.* 2008) or by shape preferred orientation (SPO) of isotropic materials with contrasting elastic properties (e.g. partial melt; Kendall & Silver 1998).

A major challenge with the interpretation of seismic anisotropy observations in the deepest mantle is that the mechanism for anisotropy and its geometrical relationship with deformation patterns remain poorly understood. The lower mantle likely consists of bridgmanite ($MgSiO_3$), ferropericlase ([Mg,Fe]O) and calcium-perovskite ($CaSiO_3$, Lee *et al.* 2004). Bridgmanite likely undergoes a phase transition to post-perovskite ($MgSiO_3$) close to the CMB (Murakami *et al.* 2004), although this phase transition is strongly dependent on temperature and composition and it is unclear whether post-perovskite is present globally (e.g. Hirose 2006). Each of these minerals (except perhaps calcium perovskite) demonstrates strong single crystal anisotropy, implying that they are possible candidate mechanisms for lowermost mantle anisotropy (as summarized in Nowacki *et al.* 2011). Despite the uncertainty in the causative mechanism, the geometry of seismic anisotropy in any case likely reflects the geometry of flow and deformation at the CMB (e.g. Nowacki *et al.* 2011).

The lowermost mantle beneath Iceland is distinguished by low shear velocities (e.g. Simmons *et al.* 2010) and by the presence of a ULVZ. Studies of the seismic structure of the lowermost mantle beneath Iceland have found evidence for a plume-like upwelling that originates at the base of the mantle (e.g. He *et al.* 2015; Yuan & Romanowicz 2017). He *et al.* (2015) examined differential travel time residuals of phases such as ScS-S that sampled the lower mantle beneath the Iceland hotspot and carried out detailed 3-D waveform modelling to understand the seismic structure of the lowermost mantle. They found evidence for a mushroom-shaped low-velocity structure at the base of the mantle beneath Iceland, which they inferred to be the root of an upwelling thermochemical plume, with the surrounding mantle exhibiting faster velocities. Yuan & Romanowicz (2017) examined the ULVZ beneath Iceland in detail by applying forward modelling of $S_{\rm diff}$ phases (shear waves diffracted at the CMB) to constrain the ULVZ geometry. Their results suggest a quasi-axisymmetric (cylindrically symmetric) ULVZ extending approximately 15 km above the CMB. Their best-fitting model has an axis of symmetry close to vertical and suggest a melt fraction of 10-20 per cent at the base of the mantle. Yuan & Romanowicz (2017) further suggest the ULVZ's location with respect to the tomographically imaged Iceland plume (French & Romanowicz 2015) implies a dynamic connection between lowermost mantle structures and surface volcanism, and posit a cylindrically symmetric upwelling in D$''$ beneath Iceland. Both the work of He *et al.* (2015) and Yuan & Romanowicz (2017) suggest a general flow regime of upwelling flow at the base of a mantle plume beneath Iceland, which generally coincides geographically with the region with low seismic velocities and evidence for a ULVZ, with horizontal flow towards the upwelling in the lowermost mantle outside of the upwelling region.

With this conceptual idea of lowermost mantle flow based on the results of He *et al.* (2015) and Yuan & Romanowicz (2017) as a framework, the goal of this study is to study seismic anisotropy at the base of the mantle beneath the Iceland hotspot using differential S–ScS and SKS–SKKS splitting measurements. In theory, we would like to test whether the proposed flow geometry is consistent with observations of seismic anisotropy. However, a major practical limitation is presented by the size of the Iceland low-velocity zone and by its location with respect to global seismicity. Specifically, the small geographical extent (diameter of 800 ± 50 km) of the velocity anomalies identified by He *et al.* (2015) and Yuan & Romanowicz (2017) makes Iceland a challenging target region for shear wave splitting measurements; furthermore, as discussed below, its location with respect to source regions of large earthquakes is not particularly favorable. In this study, we employ a combination of different body wave observations of anisotropy, namely differential S–ScS and SKS–SKKS splitting measurements. Despite the practical limitations, we were able to construct a data set that samples D$''$ beneath Iceland and the surrounding region over a range of propagation directions (after, e.g. Wookey *et al.* 2005a; Creasy *et al.* 2017). We find evidence for a distinctive anisotropic signature in D$''$, geographically coincident with a low shear velocity anomaly and with the presence of a ULVZ. While our data set is relatively small, measurements for sets of individual S–ScS raypaths are consistent, and show a clear transition in anisotropic geometry between the region of D$''$ directly beneath Iceland and regions adjacent to it. While our measurements cannot uniquely constrain a mantle flow regime, we carried out simple forward modelling for a set of plausible D$''$ anisotropy mechanisms and found that our S–ScS measurements are consistent with vertical flow at the base of the mantle beneath the Iceland hotspot.

2 METHODS

2.1 Differential S–ScS splitting

To constrain lowermost mantle anisotropy with ScS splitting measurements, we first sought to identify suitably located stations with demonstrated simple or weak upper mantle anisotropy based on SKS splitting (e.g. Lynner & Long 2014). Upper mantle corrections for our stations, discussed further below, are shown in Tables S1–S4.

To isolate the lowermost mantle component, the S–ScS differential splitting method (Wookey *et al.* 2005a) systematically corrects for the effect of anisotropy in the upper mantle close to the source and receiver and attributes the remaining signal to anisotropy in the lowermost mantle. Our measurement approach was to first correct the measured S and ScS phases for the effect of upper mantle anisotropy on the receiver side, as reflected in SKS measurements made over a range of backazimuths. Next, we measured the shear wave splitting parameters of direct S, representing the upper mantle component on the source side. Once the contributions to splitting from the upper mantle on the source and receiver side have been characterized, the third step was to implement a grid search to find the best fitting splitting parameters ϕ and δt due to D$''$ anisotropy, by applying corrections for the source-side splitting to the ScS phase in the proper sequence (Wookey *et al.* 2005a). The grid search includes all possible fast directions and delay times up to 6 s (example illustrated in Fig. 1). Following Wookey *et al.* (2005a), we applied our differential S–ScS measurements to phases measured at epicentral distances of $\Delta = 60^\circ - 80^\circ$ (see Table S5). Over this distance range, S and ScS have similar raypaths in the upper mantle at the source and receiver side. Direct S turns in the mantle above D$''$, avoiding the effects of D$''$ anisotropy. We applied a bandpass filter to all waveforms, retaining frequencies between 0.04 and 0.13 Hz. This filter was chosen to minimize interference from microseismic noise, as well as to be generally consistent with the choice of filter parameters for measurements of SKS phases that were used to correct the waveforms for upper mantle anisotropy. Our filter parameters are identical to those in several previous studies of differential S–ScS splitting (e.g. Ford *et al.* 2015; Creasy *et al.* 2017), although some studies that have used this technique have used larger values for the high frequency cutoff (e.g. Wookey *et al.* 2005a; Nowacki *et al.* 2010). We measured splitting parameters δt and ϕ of SKS phases using the transverse component minimization method as implemented in SplitLab (Wüstefeld *et al.* 2008) and ScS splitting parameters using also eigenvalue minimization method as implemented in SHEBA (Wüstefeld *et al.* 2010).

We identified a set of paths from earthquakes in and around the Mediterranean whose ScS bounce points sample the lowermost mantle in the region beneath and adjacent to the Iceland hotspot (Fig. 2). We used stations of the Yellowknife Array (YKA) and Portable Observatories for Lithosphere Analysis and Research Investigating Seismicity (POLARIS) in Canada, along with a set of stations in eastern Canada and the northeastern United States used in the work of He *et al.* (2015). We took several steps to obtain accurate upper mantle corrections and ensure that SKS splitting patterns reflect simple upper mantle anisotropy. We made new measurements of SKS splitting beneath stations YKW1-4 over multiple azimuths. We used events with $M_\mathrm{w} > 5.7$ at epicentral distances of $\Delta = 90^\circ - 127^\circ$. For stations of the POLARIS network and stations used in He *et al.* (2015) we relied on previously published SKS splitting parameters (Table S6), but we restricted our choice of stations to those which displayed simple upper mantle anisotropy patterns, with little or no variability in apparent splitting with backazimuth, and good backazimuthal coverage. Upper mantle anisotropy splitting parameters for POLARIS and other stations came from Bostock & Cassidy (1995), Barruol *et al.* (1997), Eaton *et al.* (2004), Benoit *et al.* (2013), Yang *et al.* (2017) and Chen *et al.* (2018).

We obtained on average 27 high-quality SKS splitting measurements for the Yellowknife stations and found consistent splitting parameters over a range of backazimuths, suggesting one layer of simple upper mantle anisotropy (individual station results in Tables S1–S4). The simplicity in the SKS splitting patterns further suggests that these measurements are not contaminated by lowermost mantle anisotropy beneath Canada (for a detailed discussion of possible contamination of SKS splitting patterns due to lowermost mantle structure, see Lynner & Long 2012). We next calculated average SKS splitting parameters beneath each station to use as receiver-side upper mantle corrections. We found that our average SKS splitting parameters were generally consistent across all Yellowknife stations (see Table S5), as might be expected, since they are all located within a distance of less than 30 km. They are also similar to previous splitting measurements from Wookey *et al.* (2005a). We note that we used averaged splitting parameters across all YKA stations to correct YKW4 measurements, as this station had the lowest number of measurements.

We applied the differential S–ScS splitting procedure described above to obtain splitting parameters (ϕ, δt) of the ScS phase due to lowermost mantle anisotropy. For interpretation, the measured fast directions (ϕ) in the geographic reference coordinate system were transformed into a ray-centred reference frame (ϕ'), as shown in Fig. 2(a) (after Nowacki *et al.* 2010). Following previous studies (Wookey *et al.* 2005a; Nowacki *et al.* 2010; Creasy *et al.* 2017), this coordinate transformation assumes a nearly horizontal ray path of the ScS phase in the lowermost mantle. Thus $\phi' = (backazimuth) - \phi$, defines the angle between ϕ and the vertical. When $\phi' = 90^\circ$, it indicates a horizontal fast axis, while $\phi' = 0^\circ$ indicates a vertical fast axis.

In total, 107 events measured at YKA, POLARIS, and other stations fit our geometrical limitations. However, our quality control prevented us from using more than 15 high-quality splitting measurements for further interpretation. Specifically, we discarded events showing a low SNR, and in all cases verified the ScS phase was clearly distinguishable from pS, sS, PS and other interfering phases arriving at a similar time as the ScS phase, ensuring a clear waveform. In this process, we paid particular attention to potential contamination from PS, and discarded events for which the predicted PS and S or ScS arrival times were closer than ≈ 10 s. We note that for shallow events, some contamination of the S and ScS waveforms from depth phases (sScS or sS) is theoretically possible, even though we avoided seismograms with obvious signs of waveform contamination. However, we expect depth phases to experience nearly identical splitting as the main phases, as any 'extra' splitting experienced by the upgoing leg of hypothetical depth phases to be negligible for shallow events. Therefore, contamination from depth phases, even if it occurs, is not expected to change the splitting parameter estimates. After applying the differential S–ScS splitting procedure, only results leading to a linear corrected particle motion for S and ScS phase and yielding consistent results from the eigenvalue minimization and rotation correlation methods were retained (with differences between the methods of less than $\phi = \pm 20^\circ$, $\delta t = 0.5$ s). Waveforms and diagnostic plots for each of our differential S–ScS splitting results are shown in the Figs S1–S15. We note that while in these figures we show horizontal components in the N–E coordinate system, we also examined the waveforms in the R–T coordinate system during our quality control procedures. The choice of horizontal component coordinate system for generating the figures is arbitrary, and the splitting parameter estimates are independent of the choice of horizontal coordinate system used for plotting.

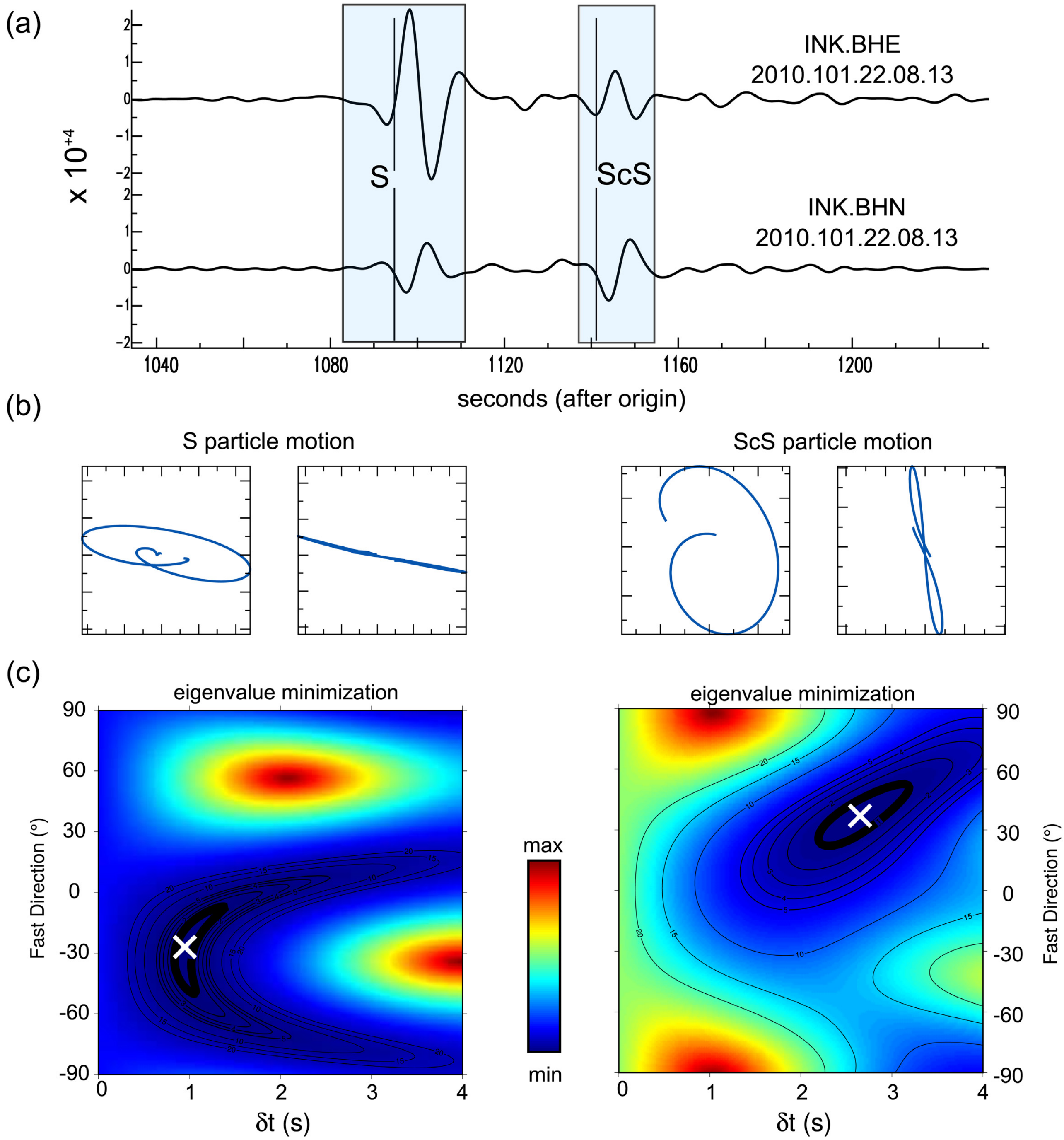

Figure 1. (a) Horizontal component of motion of the event 2010.101.22.08.13 recorded at the station INK of the Canadian National Seismograph Network and filtered using a bandpass of 0.04–0.13 Hz. The time windows used in the analysis of shear wave splitting for S and ScS are indicated by light blue colour, while theoretical marks for S and ScS using the iasp91 model (Kennett & Engdahl 1991) are indicated by the black bars. (b) elliptical and linearized particle motion for S (left-hand panel) and ScS (right-hand panel) before and after the analysis. (c) Normalized error surface plots of the eigenvalue minimization method (Silver & Chan (1991)) and splitting parameters that best linearize the particle motion (white cross) with their 95 per cent interval of confidence shown by the thick black contour line.

2.2 Differential SKS–SKKS splitting

Differences in the splitting of SKS and SKKS phases for the same event-station pair provide evidence for a contribution from lowermost mantle anisotropy to one or both phases, assuming the bulk of the lower mantle can be considered to be isotropic (e.g. Wang & Wen 2004; Lynner & Long 2014; Deng *et al.* 2017). This method does not need to explicitly consider the contributions to splitting from upper mantle anisotropy, since SKS and SKKS sample the upper mantle in nearly the same way (Fig. 3). Significantly different splitting parameters (ϕ, δt and/or splitting intensity) of SKS and SKKS phases are interpreted as reflecting a contribution from lowermost mantle anisotropy to the splitting of one or both phases. This difference could be due either to lateral gradients in lowermost mantle anisotropy, or to differences in path length and/or propagation

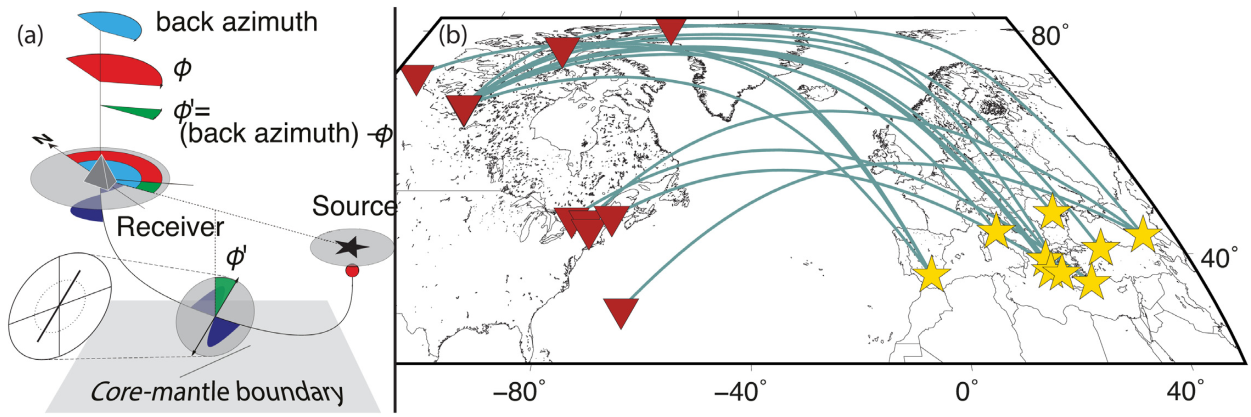

Figure 2. (a) Schematic diagram showing the geometrical relationship between ϕ and ϕ' from Nowacki *et al.* (2010). For ScS propagation in D$''$, we assume a nearly horizontal raypath, and thus ϕ'=*(backazimuth)*-ϕ describes the fast direction measured from the vertical. (b) Map of raypaths (grey lines) for our differential S–ScS splitting measurements, from events (yellow stars) in and around the Mediterranean measured at the different stations of YKA and POLARIS (red triangles).

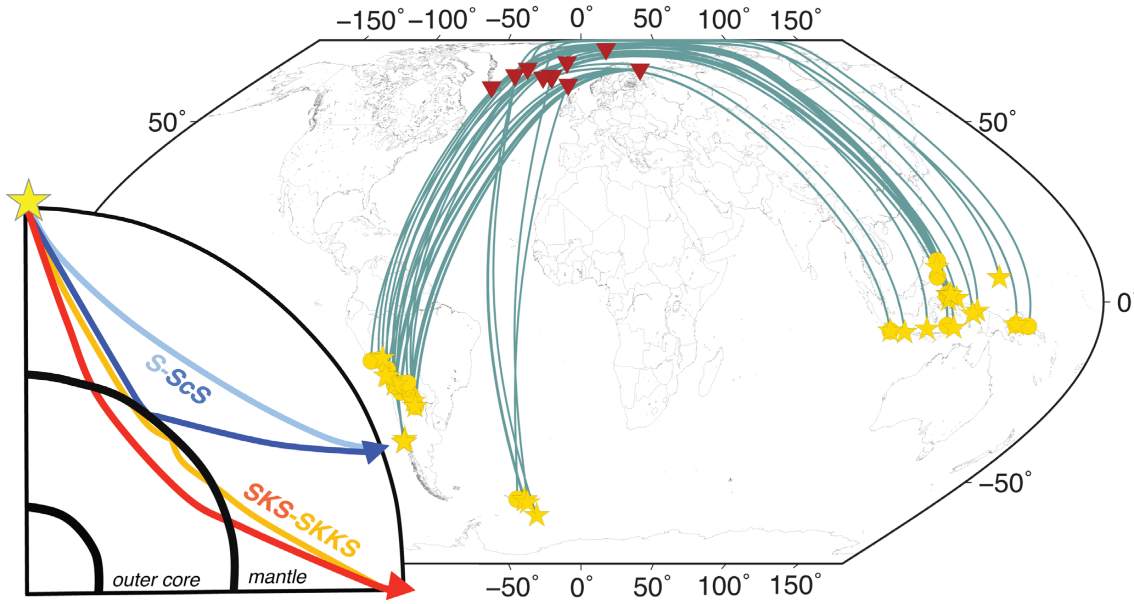

Figure 3. Events (yellow circles or stars), stations (red triangles) and ray paths (grey lines) used for SKS–SKKS splitting analysis. Events that led to satisfactory (quality B) splitting intensity measurements are depicted as yellow circles; events that led to high-quality (quality A) measurements as yellow stars. Inset shows a schematic diagram from Creasy *et al.* (2017) showing the ray paths (along a planar cross-section) of the SKS, SKKS, S and ScS used in this study.

direction through the anisotropic layer (with SKKS having a longer path through D$''$: see Fig. 3). However, SKS–SKKS differential splitting measurements alone cannot constrain the geometry of the anisotropy without careful removal of upper mantle contributions (e.g. Lynner & Long 2014).

Different studies of differential SKS–SKKS splitting take different approaches to the question of whether or not to explicitly correct the waveforms for the effect of upper mantle anisotropy. One approach is to carefully select stations with relatively simple and well-constrained upper mantle anisotropy patterns, and to correct the waveforms for the effect of upper mantle splitting (e.g. Lynner & Long 2014; Ford *et al.* 2015; Long & Lynner 2015). When this approach is taken, explicit estimates of D$''$-associated splitting of SK(K)S phases can be obtained. The downside of this approach, however, is that stations must be carefully selected for simple upper mantle anisotropy patterns; since only a small fraction of stations typically meets these criteria, the resulting data sets may be small. A second approach is to maximize the number of stations that are used in the analysis by allowing stations that have complex upper mantle anisotropy signatures, and looking only for differences in splitting between pairs of SKS and SKKS phases (e.g. Long 2009; Creasy *et al.* 2017; Deng *et al.* 2017). This approach generally leads to larger data sets, but with this strategy estimates of the D$''$-associated portion of the splitting signal cannot be obtained. In designing our Iceland study, we weighed the potential tradeoffs associated with each approach, and because many of the stations located in our study area are associated with complex upper mantle anisotropy, we decided against implementing explicit upper mantle corrections here.

We used 17 permanent and temporary stations in Iceland, Greenland and Europe with high-quality data and a wide backazimuthal coverage for our target region (Fig. 3). We selected events of magnitude $M_w > 5.7$ in an epicentral distance range between $\Delta = 100° - 126°$. We applied the same bandpass filter to all waveforms as for the S–ScS splitting analysis (retaining frequencies between 0.04 and 0.13 Hz). We retained seismograms exhibiting high-quality arrivals for both SKS and SKKS, with high SNR and good waveform quality, determined by visual inspection (e.g. Fig. 4). Following recent work on lowermost mantle anisotropy beneath the eastern Pacific (Deng *et al.* 2017) we focused on measuring the shear wave splitting intensity for SKS and SKKS phases, as described below. This choice of measurement strategy is based on the finding that splitting intensity discrepancies, rather than discrepancies in measured fast direction and/or delay time, represent a more robust measurement for noisy data or relatively weak differential splitting. We carried out data preprocessing and splitting intensity measurements using a modified version of SplitLab (Wüstefeld *et al.* 2008), a shear wave splitting software toolkit for Matlab. Measurements of splitting intensity (SI), introduced by Chevrot (2000), were carried out using SplitLab modifications introduced in Deng *et al.* (2017). The SI is a measure of the relative energy on the transverse component seismogram, given by Chevrot (2000):

$$SI = -2\frac{T(t)R'(t)}{|R'(t)|^2}, \tag{1}$$

where the transverse component, $T(t)$, is projected onto the time derivative of the radial component, $R^{'}(t)$. This projection is normalized by the squared magnitude $R^{'}(t)$. For the case of a single layer of anisotropy, the transverse component energy is related to the traditional splitting parameters δt and ϕ via the following equation:

$$T(t) \approx -\frac{1}{2}(\delta t \sin(2(\alpha - \phi)))R'(t), \tag{2}$$

where α defines the polarization of the incoming wave and ϕ the fast direction. This implies the SI is related to δt and ϕ via the relationship:

$$SI \approx \delta t \sin(2(\alpha - \phi)). \tag{3}$$

We compute the 95 per cent confidence range following the formulation of the mean square error from appendix B in Chevrot (2000) as implemented in Deng *et al.* (2017). Differential SKS–SKKS splitting intensity measurements, along with error estimates, are shown in Tables S7–S23.

A key advantage of the SI method for SKS–SKKS splitting discrepancy studies, as discussed in detail by Deng *et al.* (2017), is that the definition of a null (non-split) measurement does not require a particular combination of diagnostic parameter values and waveform behavior. Instead, null phases exhibit SI values near zero, corresponding to linear or nearly linear uncorrected particle motion.

3 RESULTS

3.1 S–ScS results

Our differential S–ScS analysis yielded 15 measurements of ScS splitting due to lowermost mantle anisotropy (Fig. 5). Waveforms and diagnostic plots for all ScS splitting measurements are shown in Figs S1–S15, and all ScS splitting measurements are shown in Table S5. While this is a relatively low number of measurements (limited mainly by the relatively sparse seismicity in the source region), each measurement passes our quality checks, and measurements for adjacent raypaths are consistent, lending additional confidence to our results. A clear geographical pattern is readily apparent (Fig. 5), in which one group of raypaths (R1) samples the lowermost mantle within or just adjacent to the low-velocity region of the mantle directly beneath Iceland, and has a consistent set of $\phi^{'}$ directions being nearly vertical (implying $V_{SV} > V_{SH}$). In contrast, the second and third group of raypaths (R2 and R3) sample well outside the low-velocity region, and instead sample the lowermost mantle to the north and south of Iceland. R2 and R3 generally exhibit $\phi^{'}$ values that are nearly horizontal, implying ($V_{SH} > V_{SV}$). We note that there is one measurement (out of four) in group R2 that contrasts with the nearly horizontal $\phi^{'}$ values generally observed for this group; this measurement is marked in blue in Fig. 5 and has a more nearly vertical $\phi^{'}$ value. The CMB bounce point for this phase lies substantially to the south and east of those for the rest of the measurements in this group, and the measurement samples the edge of another low-velocity anomaly that is distinct from the Iceland anomaly (Fig. 5). We speculate that this single measurement may be sampling a local anomaly in lowermost mantle anisotropy that is colocated with the velocity anomaly.

The splitting delay times that we document in this study (Table S5) range from 1.1 to 5.8 s. The upper end of this range is larger than is typical in studies of lowermost mantle anisotropy that rely on ScS splitting, in which delay times generally range from 1-3 s (e.g. Wookey *et al.* 2005a; Ford *et al.* 2015; Creasy *et al.* 2017; Rao *et al.* 2017). However, only four of our 15 measurements are larger than 3 s, and the average δt in our study is 2.9 s, which is in line (although on the high end) with the range reported in previous studies.

As in any study of differential ScS-S splitting, the quality of the individual measurements is a concern, since the method relies on a series of corrections for source-side and receiver-side anisotropy in the upper mantle. Furthermore, because of the relatively limited number of measurements in our differential S–ScS splitting data set (15), it is crucial to ensure the quality and reliability of individual measurements. For some of the measurements in our data set, the SNR values for the ScS phases are not particularly high, although in all cases we have followed the quality control criteria and SNR thresholds described above. In order to characterize the quality of each measurement, we have assigned each measurement a quality ranking (A versus B), with quality A results having higher SNRs, more clearly elliptical particle motion due to D$^{''}$-associated splitting, more clearly linearized particle motions after correction for splitting, and generally smaller upper mantle receiver-side corrections (since inaccurate upper mantle corrections are a source of error in the measurements). The quality rankings for each of the 15 measurements in our differential S–ScS splitting data set can be found in Table S5.

3.2 SKS–SKKS results

Our analysis yielded 59 well-constrained SKS–SKKS splitting pairs sampling the lowermost mantle beneath Iceland and the surrounding region, as shown in Fig. 6 and Tables S7–S23. Of those, we identified 28 SKS–SKKS pairs as discrepant. A pair was defined as discrepant if $\Delta SI = |SI_{SKS} - SI_{SKKS}| \geq 0.3$ and the 95 per cent confidence regions of measured SI values did not overlap. If $\Delta SI \geq 0.3$ and the 95 per cent confidence intervals did overlap, the measurement was classified as ambiguous. If $\Delta SI < 0.3$ the pair was defined as non-discrepant. For the case with no splitting discrepancy, there is no reason to infer a contribution from the lowermost mantle (although such a contribution cannot be definitively ruled out in this case). For the case where a splitting discrepancy is observed, one can confidently infer a contribution from lowermost mantle anisotropy to one or both phases (Wang & Wen 2004). An example

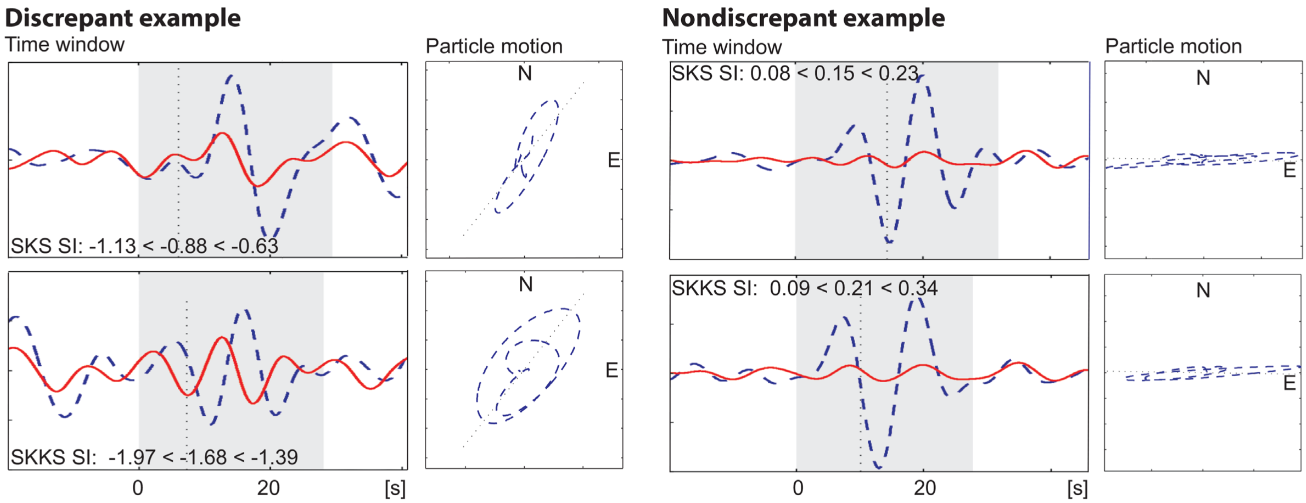

Figure 4. Examples of differential SKS–SKKS splitting intensity measurements. Left-hand panels: an example of discrepant SKS–SKKS splitting measured at station KOLL for an event on 11 September 2008 in a backazimuth of 38.2°. The amplitude ratio between transverse (solid red) and radial (dashed blue) component for SKS (top panels) and SKKS (bottom panels) clearly differs; measured values of splitting intensity and their formal errors are shown at the bottom. The corresponding particle motion diagrams (particle motion shown with dashed blue lines in central panels) show a more elliptical motion Right-hand panels: an example of a non-discrepant measurement recorded at station LVZ for an event on 25 August 2006 coming from a backazimuth of 270.9°. The transverse component pulse shapes and amplitudes for the SKS and SKKS phases look very similar and the particle motion is almost linear in both cases.

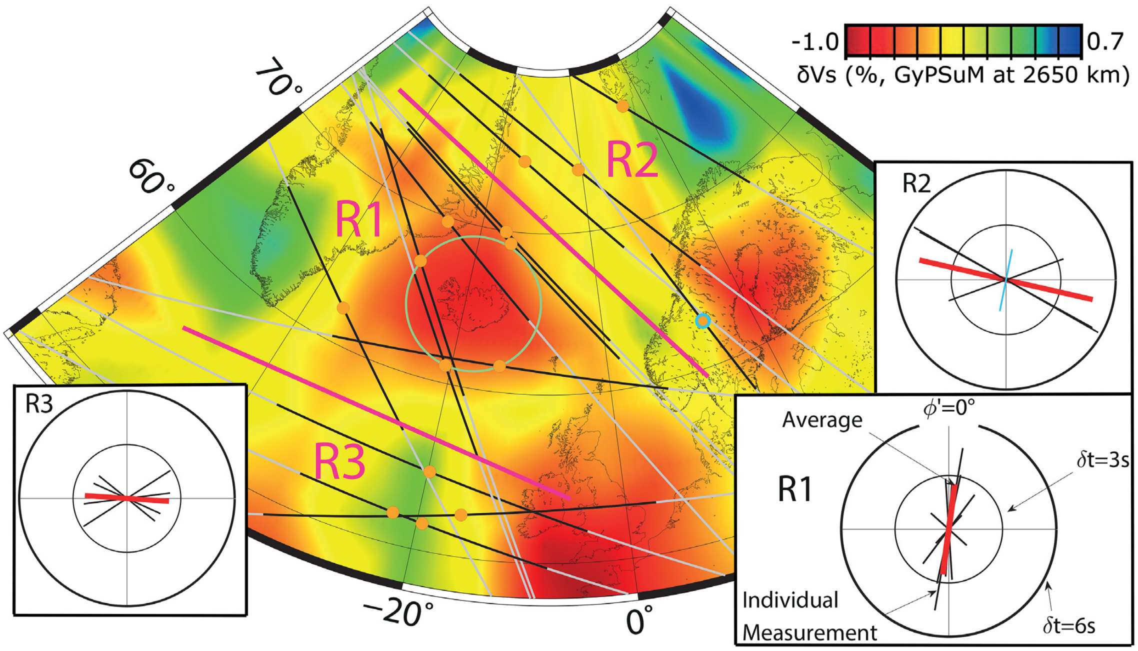

Figure 5. Results of differential S–ScS splitting analysis. Background colours depict *S*-wave velocity perturbations at a depth of 2650 km from GyPSuM tomography model. The light green circle indicates the approximate region of ULVZ material identified by Yuan & Romanowicz (2017). Lines show raypaths (black lines inside D″ region, grey lines outside) for the 15 ScS measurements with quality A and B (see Table S5). Yellow circles indicate the bounce points of the ScS phase off the CMB. The eight ray paths in R2 and R3 sample the lowermost mantle well outside of the ULVZ location identified by Yuan & Romanowicz (2017) (green circle). The seven raypaths in R1 sample the lowermost mantle either inside or just at the edge of the ULVZ region. The regions are separated by magenta lines. The D″-associated fast axis ϕ' and time delay δt are shown by the insets labeled R1, R2 and R3. The angles of the lines show ϕ' of the individual measurements (black) and the averaged measurements of the particular region (red). One measurement in R2 is marked with light blue (contour of bounce point and line in inset). This measurement was not used for the calculation of the R2 average (for further discussion see Fig. 3.1). The length of the line indicates δt. ϕ' rotates from ≈90°and outside our target region to ≈10° at the edge of Iceland plume.

of a discrepant and a non-discrepant SKS–SKKS pair is shown in Fig. 4.

As with most SKS–SKKS splitting discrepancy data sets, our observations show considerable scatter (e.g. Lynner & Long 2014; Deng *et al.* 2017), and few if any discernable geographical patterns are evident in Fig. 6. We did observe that nearly all the SKS–SKKS pairs measured at seismic stations on Iceland sample D″ well to the north and east of Iceland, far away from the low-velocity anomaly, and were found to be non-discrepant. For these pairs, the recorded

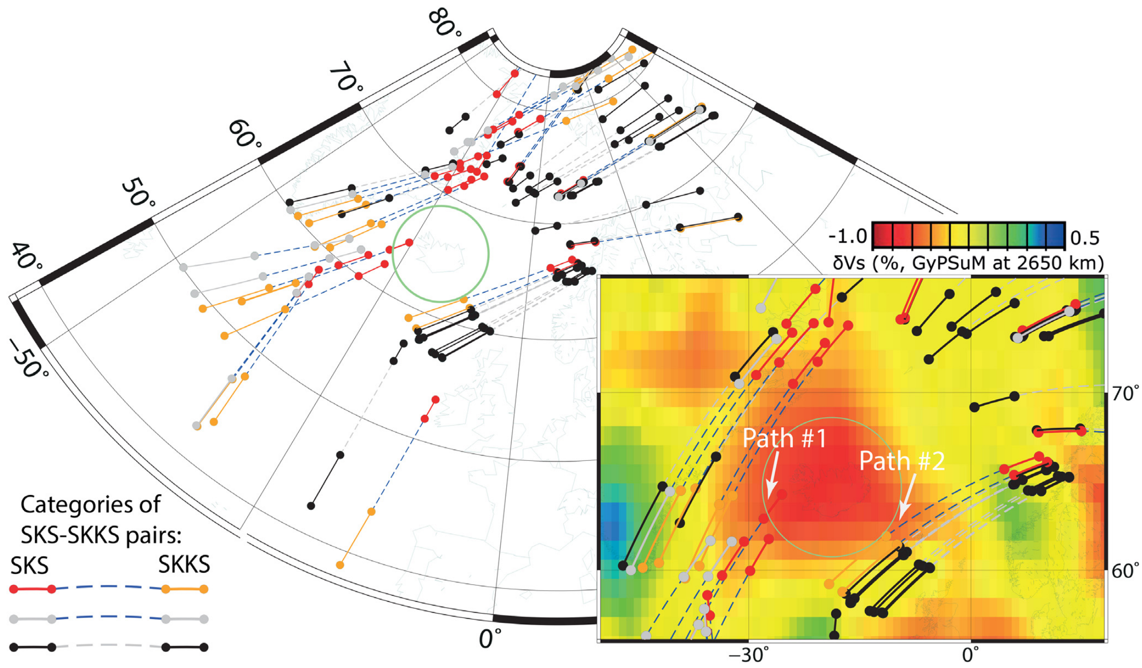

Figure 6. Map of SKS–SKKS splitting discrepancy results close to Iceland (59 pairs in total, where many overlap each other). Dots show pierce points (circles), calculated via TauP (Crotwell *et al.* 1999) of SKS and SKKS phases at top and bottom of the D″, assuming a 250 km thick D″ layer. (Dashed lines connect the corresponding SKS–SKKS pairs for the same earthquake-receiver pair. Colours indicate three different categories of splitting behaviour: non-discrepant pairs (black) are those for which $\Delta SI < 0.3$, discrepant pairs (red for SKS and orange for SKKS) are those for which $\Delta SI \geq 0.3$, with no overlap between the 95 per cent confidence regions on SI for SKS and SKKS. Ambiguous (grey) are those pairs for which $\Delta SI \geq 0.3$ but the 95 per cent confidence range of SKS and SKKS measurements overlap. The light green circle indicates the approximate region of ULVZ material identified by Yuan & Romanowicz (2017). Inset: Map of results, zoomed in on the region immediately around Iceland and with background colours depicting (isotropic) S-wave velocity perturbations from the GyPSuM tomography model at a depth of 2650 km (Simmons *et al.* 2010).

SKS and SKKS waveforms are similar and do not require a contribution from lowermost mantle. In contrast, pairs sampling the lowermost mantle just outside the low-velocity region (particularly to the north and to the southwest), were more likely to show discrepancies, suggesting a contribution to the splitting of one or both phases from D″ anisotropy. A particularly interesting pattern was observed for a set of pairs with nearly parallel raypaths measured at station LVZ, whose SKKS paths sample the lowermost mantle just to the southeast of the Iceland low-velocity region (shown in Fig. 6 inset, see path #2). Most of these pairs are non-discrepant (black lines Fig. 6), but the two phases sampling closest to the Iceland low-velocity region show discrepancies. In general, however, the SKS–SKKS splitting discrepancies that we document in this study are distributed throughout the study area, with little or no correlation with geographic features such as the lowermost mantle low velocity zone.

4 DISCUSSION

4.1 Interpretation of differential splitting measurements for D″ anisotropy

The interpretation of shear wave splitting measurements in terms of D″ anisotropy must be conducted cautiously, because contributions from anisotropy in the upper mantle must be carefully accounted for. The interpretation of splitting data sets with limited azimuthal coverage is non-unique, and possible waveform effects other than anisotropy must be considered. We emphasize that our measurement procedure for both SKS–SKKS and S–ScS differential splitting encompasses several precautions to avoid interpreting noise or splitting due to upper mantle anisotropy in terms of D″ structure. With the SK(K)S results, we followed previous work (Deng *et al.* 2017) and evaluated the shape of the transverse component waveform in our SI measurements, ascertaining the shape of the transverse component resembled the time derivative of the radial component. This step rules out the possibility of transverse energy caused by scattering due to isotropic heterogeneity (e.g. Lynner & Long 2014) or by dramatic lateral variations in complex anisotropy or isotropic wavespeed structure at the base of the mantle (see, e.g. Restivo & Helffrich 2006). Only relatively large ($\Delta SI \geq 0.3$) differences in the splitting parameters of SKS and SKKS indicating a contribution from D″ were interpreted, minimizing the chances of misinterpreting finite frequency effects due to upper mantle anisotropic structure (Lin *et al.* 2014).

As in many studies of differential SKS–SKKS splitting, we cannot directly interpret our results in terms of the anisotropic geometry in the D″ region, nor can we carry out explicit corrections of measured splitting intensity to account for differences in path length between SKS and SKKS. Nearly all of the stations used in our SKS–SKKS analysis exhibit relatively complicated upper mantle anisotropy, with backazimuthal variability in apparent splitting parameters (see Tables S7–S23). In some SKS–SKKS discrepancy studies, relatively simple upper mantle anisotropy beneath the stations can be explicitly accounted for, with waveforms corrected for the effect of upper mantle splitting and the residual splitting directly attributed to D″ (e.g. Lynner & Long 2014). In this study, however, the complex upper mantle anisotropy beneath our stations precluded this approach. Rather, the interpretation of our SKS–SKKS discrepancy measurements focuses on the inference a contribution to the splitting of one or both phases from anisotropy in the lowermost mantle. This could be due to a lateral gradient in seismic anisotropy near the CMB between the mantle volume sampled by SKS and that sampled by the corresponding SKKS, or it could be due to a difference in path length or propagation directions between SKS and SKKS phases through the D″ layer in the presence of homogeneous anisotropy. Therefore, we use the presence and geographical distribution of discrepant SKS–SKKS splitting as a likely indicator the presence of seismic anisotropy in D″; this evidence for lowermost mantle anisotropy is complementary to that provided by our ScS splitting results.

of lateral gradients in seismic anisotropy near the CMB between the mantle volume sampled by SKS and that sampled by the corresponding SKKS, and/or a difference in path length or propagation directions between SKS and SKKS phases through the D″ layer in the presence of homogeneous anisotropy. Therefore, we use the presence and geographical distribution of discrepant SKS–SKKS splitting as a likely indicator of complex and laterally variable anisotropy in D″.

As with SKS–SKKS splitting, there are some caveats to our interpretation of ScS splitting measurements in terms of D″ structure. ScS waves do not travel exactly horizontally through the D″ layer, although this is a commonly made assumption (e.g. Wookey *et al.* 2005a; Nowacki *et al.* 2010; Creasy *et al.* 2017). While our forward modelling procedure, described below, does take into account the deviation from horizontal propagation on the downgoing and upgoing ScS legs, our measurement procedure itself does not, and implicitly assumes a single layer of anisotropy (consistent with a simplified, horizontal propagation direction). Furthermore, our analysis does not explicitly take into account differences in epicentral distance among the measurements in our data set. Small differences in incidence angle may result in minor differences in splitting due solely to ray path geometry. However, our ScS splitting data set does not show any correlation between splitting parameters and epicentral distance (Table S5). Instead, the drastic rotation in fast direction in our ScS observations is controlled by the geographic distribution of Iceland versus non-Iceland paths.

Both our measurement methods and our forward modelling framework (described below) rely on a ray theoretical approximation and explicitly disregard finite frequency effects; this is a considerable limitation of our study, and future work that interprets our measurements in a finite-frequency framework is necessary. It is well known that isotropic structural variations (including the solid–liquid contrast across the CMB) can affect the waveforms of shear phases sampling D″ when finite frequency effects are taken into account (e.g. Kawai & Geller 2010; Parisi *et al.* 2018). However, the extent to which waveform distortion can mimic shear wave splitting has been debated in the literature. Some workers (Kawai & Geller 2010) have argued that CMB effects can distort SV and SH waveforms to such an extent that shear wave splitting observations can never be interpreted in terms of lowermost mantle anisotropy. However, recent modelling work by Nowacki & Wookey (2016) demonstrated that isotropic models do not produce apparent splitting of ScS phases when using the S–ScS differential splitting method of Wookey *et al.* (2005a). The ray theoretical approach to both measurements and observations that we use in this paper, while common in observational studies of D″ anisotropy, must be validated through future work that explicitly incorporates finite frequency effects in observations and modelling of D″-associated shear wave splitting. This work is particularly crucial, given that Nowacki & Wookey (2016) found that while ray theory often makes sufficiently accurate splitting predictions for relatively simple lowermost mantle anisotropy models, finite-frequency effects are increasingly important for more complex anisotropic scenarios. A major challenge with full-wave methodologies for modelling lowermost mantle splitting observations, however, is the computational expense, which is considerable for global simulations down to the relevant periods (Nowacki & Wookey 2016). Despite the challenges, moving studies of lowermost mantle anisotropy towards a consideration of full-wave effects on shear wave splitting is a necessary next step.

4.2 Inferences on D″ anisotropic structure beneath Iceland

With these caveats in mind, we use our differential S–ScS and SKS–SKKS splitting observations to draw conclusions about the possible geometry of anisotropy in the lowermost mantle beneath Iceland. Strong support for the presence of lateral changes in anisotropy across the Iceland hotspot is provided by our S–ScS shear wave splitting measurements, showing a marked difference in D″-associated splitting for paths sampling within and to the north of the low-velocity region (Group R1 in Fig. 5) compared with paths propagating well outside (Groups R2 and R3). Our S–ScS measurements suggest a $V_{SV} > V_{SH}$ anisotropic geometry beneath the Iceland hotspot, with a geometry closer to $V_{SH} > V_{SV}$ outside this region.

Additional support for the presence of D″ anisotropy directly beneath Iceland is also provided by our SKS–SKKS splitting data set, although in this case the interpretation of the data is more tentative. The SKS–SKKS discrepancy data are geographically scattered (Fig. 6), and a plot of splitting intensity difference as a function of distance from the centre of the plume (Fig. S16) shows only a weak relationship for entire data set. We also tested for possible relationships between differences in relative arrival times for SKS–SKKS phases, differences in splitting intensity, distance from the centre of the plume, and the relative travel time (Figs S16–S18). However, any relationships are weak for the full data set, likely because none of the SKS–SKKS pairs directly sample the central portion of the low-velocity zone beneath Iceland (Fig. 6).

We conclude that our observations of widespread SKS–SKKS discrepancies for pairs sampling the region directly surrounding the Iceland hotspot near the region of low seismic velocities and inferred ULVZ material (Yuan & Romanowicz 2017), is generally consistent with the idea that there is significant seismic anisotropy in the lowermost mantle there. One possible explanation for SKS–SKKS splitting discrepancies is the presence of local lateral gradients in anisotropic structure in this region, although another explanation invokes a homogeneous region of anisotropy, with differences in splitting between the phases caused by differences in path length and/or propagation direction. Therefore, our observation of widespread SKS–SKKS discrepancies can be viewed as consistent with the inference from the differential S–ScS splitting measurements that there is a transition in anisotropy geometry directly beneath Iceland, compared with the lowermost mantle surrounding the plume region. However, this line of evidence is somewhat circumstantial, and the spatial patterns in the SKS–SKKS splitting intensity discrepancy data are much less clear cut than those in our S–ScS measurements. While the SKS–SKKS discrepancies lack a strong constraint on the nature of lowermost mantle anisotropy beneath Iceland, they are generally consistent with the presence of anisotropy, and with the inference from the ScS splitting patterns that there are lateral transitions in anisotropic structure in D″ beneath the Iceland hotspot.

4.3 Inferences on D$''$ flow beneath Iceland: forward modelling

4.3.1 Modelling approach and assumptions

Our S–ScS measurements are consistent with a lowermost mantle anisotropy geometry directly beneath Iceland that is different than the surrounding lowermost mantle. order to make specific inferences about the pattern of mantle flow associated with this transition, we must assume geometrical relationships between flow, mantle deformation, and the resulting anisotropy. Studies of D$''$ anisotropy often assume the fast direction of anisotropy in the lowermost mantle is parallel to the shear direction (e.g. Nowacki *et al.* 2011). However, uncertainty remains about the mineralogy of the lowermost mantle, particularly in a region of low seismic velocities potentially indicating high temperatures and the presence of partial melt. Furthermore, the dominant slip systems in individual minerals at lowermost mantle conditions, and how different materials might contribute in a polyphase aggregate, remain poorly understood (e.g. Immoor *et al.* 2018).

Despite these limitations, we can carry out a series of simple, ray theoretical forward modelling experiments to understand which plausible anisotropy scenarios are consistent with our observations. Specifically, we test whether the concept of lowermost mantle flow proposed by He *et al.* (2015) and Yuan & Romanowicz (2017), which invokes a plume-like upwelling directly beneath Iceland, is consistent with our data, under a series of simple assumptions about possible anisotropic mechanisms/geometries. This model invokes a transition from horizontal mantle flow (directed towards the base of the putative Iceland plume) outside the Iceland low-velocity region to cylindrically symmetric, vertically directed flow (upwelling) within the Iceland low-velocity region (Fig. 7). In our modelling, we assume that the difference in anisotropy we observe between the region directly beneath Iceland and the region outside it reflects a change in mantle flow direction. We emphasize, however, that other interpretations of our observations are also possible. Specifically, lateral gradients in anisotropy could be caused by lateral changes in anisotropic mechanism or mineralogy, rotation of fossilized fabric, texture inheritance across phase transitions, and/or changes in dominant slip system(s). While we cannot rule out any of these scenarios, our focus is testing whether our observations are consistent with a cylindrically symmetric upwelling at the base of the mantle.

Our forward modelling relies on a highly simplified view of mantle flow at the base of a plume, one that invokes vertical flow in the low-velocity zone beneath the plume and horizontal flow (directed inwards towards the plume centre) outside of it. We do not consider details such as the width of the plume conduit, the breadth of the plume base, and the details of the transition from horizontal to vertical flow in this study. In reality, the morphology of the upwelling, including its width, will depend strongly on thermochemical effects and on the rheology of the lowermost mantle (e.g. Lin & van Keken 2006; Samuel & Bercovici 2006), which are not well known for Iceland (or for the lowermost mantle more generally). Specifically, the distance from the centre of the plume to the region dominated by horizontal flow surrounding it is likely to vary depending on the mineralogy and rheology, potentially affecting which raypaths in our study are sampling regions of vertical or horizontal flow (or flow that is transitional between the horizontal and vertical regimes). Our intent in the present paper is not to provide an exhaustive investigation of all possible models for upwelling flow at the base of the Iceland plume; rather, we intend to test whether a simple and qualitative (but plausible) geodynamic scenario can explain the first-order aspects of our ScS splitting observations. Future work that encompasses more realistic geodynamic flow scenarios, and relies on detailed flow fields predicted by a range of models with different rheology parameters, will expand on the simple models presented here.

We carry out simple models of predicted splitting patterns for a suite of candidate elastic tensors (Fig. 1) and test whether various scenarios can reproduce our observations. Our modelling closely follows our approach in previous studies (Ford *et al.* 2015; Creasy *et al.* 2017). We assume a simplified modelling framework, in which we first consider a set of elastic tensors that are based on single-crystal elasticity of lower mantle minerals. For these tests, we assume that the elasticity of a polycrystalline aggregate exhibits a geometry (although not strength) that is similar to the elasticity of its single-crystal component (for further discussion of this assumption, see Ford *et al.* 2015). We further assume a simplified deformation geometry (illustrated in Fig. 7), with horizontal simple shear outside of the upwelling area (shear direction towards the centre of the upwelling and slip direction in direction of macroscopic shear). The cylindrical symmetry of the upwelling implies a hexagonal symmetry of anisotropy, with the dominant slip direction oriented vertically (at least in the centre of the up-welling region). We therefore average candidate elastic tensors in the horizontal directions to produce a vertical transversely isotropic medium, following Montagner & Anderson (1989), assuming the slip direction is oriented in the flow direction. Away from the centre of the plume, our simplifying assumption of hexagonal symmetry may not strictly hold.

We initially consider three possible (single-crystal) mineralogical mechanisms for anisotropy (Fig. 1), namely CPO of bridgmanite (Br) ($MgSiO_3$), ferropericlase (Fp) ([Mg,Fe]O) and post-perovskite (Ppv) ($MgSiO_3$). We assume that dislocation glide is the dominant deformation mechanism. The mineralogy of the lowermost mantle, and which mineral phase(s) make major contributions to the observed anisotropy, remain poorly known. Specifically, the depth of phase transition of bridgmanite to post-perovskite is not very well constrained and is highly dependent on temperature and composition (Cobden *et al.* 2015). In the case of a low-velocity region with ULVZ material present, such as beneath Iceland, we expect higher than average lowermost mantle temperatures ((e.g. Hernlund & McNamara 2015), and references therein). Higher temperatures would drive the Br-Ppv phase transition to higher pressures; therefore, the mineralogy in D$''$ may be dominated by bridgmanite. While the single crystal elasticity of bridgmanite is quite anisotropic (Wookey *et al.* 2005b), there is some doubt as to whether Br deforms by dislocation creep (e.g. Kraych *et al.* 2016), as opposed to a deformation mechanism that does not produce CPO. Given these uncertainties, we test both Ppv and Br as possible candidates. We also consider ferropericlase as a possible contributor; while Fp is the least abundant anisotropic phase in D$''$, it is the weakest mineral of the three (Yamazaki & Karato 2001) and the most anisotropic (Karki *et al.* 1999). Some recent work, however, has suggested that when Fp deforms with Br in a polyphase aggregate, Fp does not develop a coherent texture (Miyagi & Wenk 2016). While the potential contributions from Fp remain uncertain, we have included Fp in our tests here as a possibility.

We used single-crystal elastic tensors for Br, Ppv and Fp from Wookey *et al.* (2005b), Stackhouse *et al.* (2006), and Karki *et al.* (1999), respectively. In order to relate the flow geometry under consideration to the anisotropic geometry, knowledge (or assumptions) of the dominant slip systems in each material, along with their relative strengths, are needed. Current understanding of dominant slip

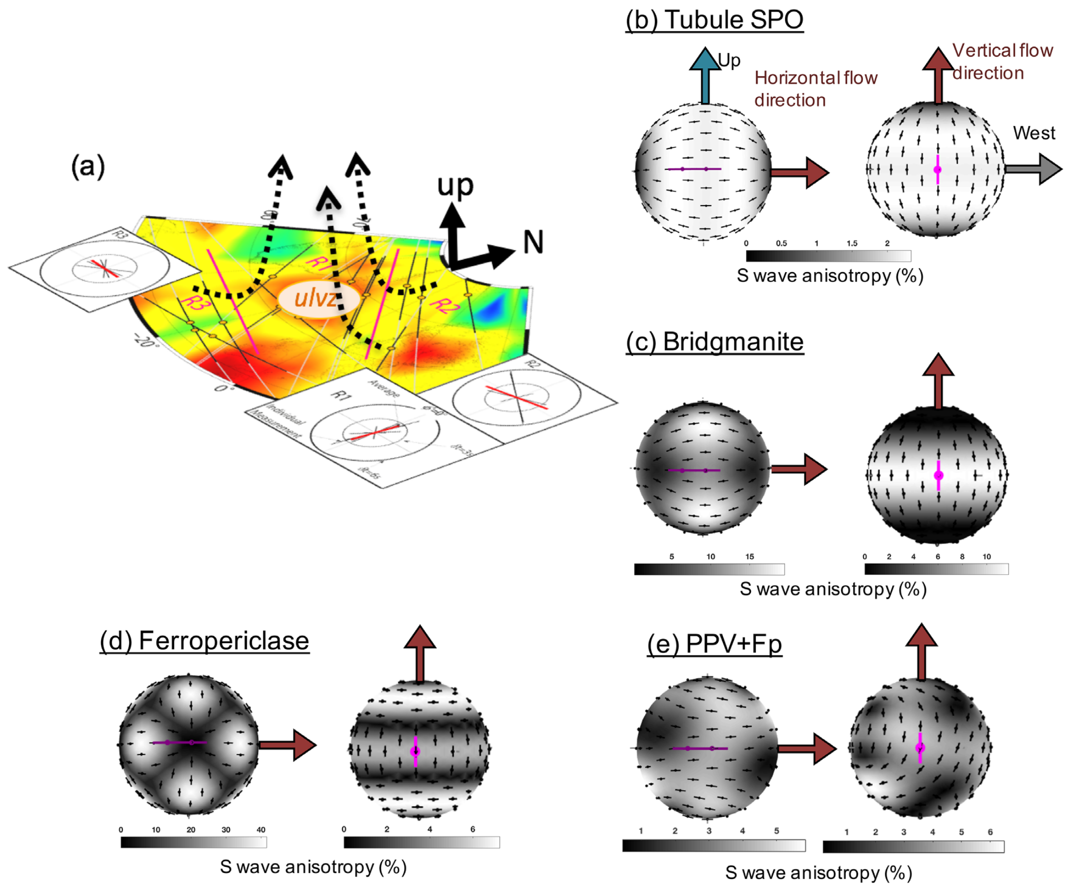

Figure 7. (a) Cartoon view of the conceptual model for mantle flow (black arrows) tested here, based on the suggestion of He *et al.* (2015) and Yuan & Romanowicz (2017), with horizontal mantle flow outside the low-velocity region and vertical in the low-velocity region. Solid arrows represent the raypaths tested here and correspond to (b)–(e). The two paths identified for ScS are from Fig. 5. Path #1 represents R1 from Fig. 5, while path #2 represents R2 and R3. (b)–(e) Splitting predictions and observations for the four successful models. Shown are spherical representations of the predicted shear wave splitting behavior as a function of propagation direction, with colour representing the strength of shear wave anisotropy and black bars showing predicted fast polarization directions. The S–ScS shear wave splitting observations are shown as light violet (assumed to propagate directly beneath the plume) and dark purple (assumed to propagate outside the plume). (b) Tubule SPO; (c) single crystal bridgmanite assuming the slip system [001](100); (d) ferropericlase assuming the slip system 1/2 <110>{110} for vertical and horizontal flow; (e) polyphase aggregate of 70 per cent Ppv and 30 per cent Fp.

Table 1. Summary of all elastic tensors used to evaluate fit with observations. Columns show the type of tensor (VPSC tensors, single-crystal, LPO based on experimental data, SPO based on effective medium averaging, or LPO based on global flow and texture models), the phase and/or constituents, and the reference. For the single-crystal tensors and VPSC tensors, the pressure and temperature conditions used in the modelling are also indicated.

Geometry	Phase	Pressure [GPa]	Temperature [K]	References
Single crystal	Br	126	2800	Wookey *et al.* (2005b)
	Ppv	136	3000	Stackhouse *et al.* (2006)
	Fp	135	3000	Karki *et al.* (1999)
VPSC tensors	Ppv	126–136	2000–3000	Walker *et al.* (2011)
	Ppv+Fp	125	2000	Tommasi *et al.* (2018)
Geometry	Phase	Notes		References
SPO[a]	0.05 vol. frac. melt	Oblate shape, MSAT/ Tubule shape, MSAT		Walker & Wookey (2012)

[a]Input values for elastic constants: $Vp_{\mathrm{matrix}} = 13.9\,\mathrm{km\,s^{-1}}$; $Vs_{\mathrm{matrix}} = 7.9\,\mathrm{km\,s^{-1}}$; $density_{\mathrm{matrix}} = 5324\,\mathrm{kg\,m^{-3}}$; $Vp_{\mathrm{inclusion}} = 7\,\mathrm{km\,s^{-1}}$; $Vs_{\mathrm{inclusion}} = 0\,\mathrm{km\,s^{-1}}$; $aspect\ ratio_{oblate} = 0.05$; $aspect\ ratio_{tubule} = 20$; volume fraction of inclusions = 0.05.

systems at lowermost mantle conditions is imperfect; however, our choice of slip systems to test is informed by recent experimental and modelling results. For single-crystal Ppv, we consider two possible dominant slip systems, [100](010) and [010](001), as suggested by Goryaeva *et al.* (2016) and Miyagi *et al.* (2010), respectively. For Br, we consider two possible dominant slip systems: [100](010) and [010](100), both suggested by Gouriet *et al.* (2014). For Fp, slip could occur on the {110} slip planes (Karato 1998); however, experiments on deformation of Fp (Girard *et al.* 2012) show at higher pressures, slip could occur instead on the 100 set of planes. Dominant slip systems are dependent on pressure, temperature and Fe content, but we only consider slip systems 1/2 <110>{110} and 1/2 <110>{100}.

We next consider a second class of possible mechanisms for D$''$ anisotropy invoking shape preferred orientation (SPO) of partially molten material aligned in a preferential direction (Kendall & Silver

1998) (Fig. 1). We consider partial melt pockets aligned in cigar-like (tubule) shapes or in flat (oblate) pancakes, as suggested by Nowacki *et al.* (2011). We assume that in the case of horizontal lateral flow along the CMB, pockets of molten material would be aligned sub-parallel to the CMB, and in the tubule case, we further assume the long axis of the tubules will be aligned in the shear direction. For the vertical flow, we assume the melt pockets would align vertically; for the oblate melt case, we averaged around a vertical rotation axis to produce a vertical transverse isotropic medium that is cylindrically symmetric. We generated melt SPO elastic tensors based on the effective medium modelling approach of Tandon & Weng (1984), using MSAT (Walker & Wookey 2012), a Matlab toolkit for manipulation of elastic tensors. For the tubule SPO case, we used an aspect ratio of 20 (following Kendall & Silver 1998) with 5 per cent volume fraction of inclusions. For oblate SPO, we consider an aspect ratio of 0.05, producing very strong seismic anisotropy with very little partial melt (20 times more than tubule SPO for the same volume of inclusions). The pattern of seismic anisotropy remains the same for the tubule case for aspect ratios greater than one; however, the strength increases. Similarly, the pattern of anisotropy remains the same for the oblate case for aspect ratios less than 0.1; however, the strength increases as well as the aspect ratio decreases. While the expected (isotropic) velocity reduction expected for the melt fraction and configuration used in our modelling will vary depending on the details of whether the melt pockets are interconnected or not, the volume fraction of partial melt in our models (5 per cent) is in line with previous studies that have sought to understand what melt fractions are needed to produce the velocities observed in ULVZ regions of the lowermost mantle (e.g. Williams & Garnero 1996; Berryman 2000; Hernlund & Jellinek 2010; Hier-Majumder & Drombosky 2016).

In addition to the models based on single-crystal elasticity and effective medium modelling of partial melt, we also test two different sets of elastic tensors that are based on a combination of geodynamic modelling (either global or regional) and modelling of texture development in polycrystalline aggregates. In the first case, we use elastic tensors derived from the modelling study of Walker *et al.* (2011), who combined a model of mantle flow and strain accumulation with a model of texturing in a Ppv aggregate. The global flow model used in Walker *et al.* (2011) does not capture the (possible) localized upwelling at the base of the plume beneath Iceland, so we do not use the flow and texture predictions from this region of the model. Instead, we use an elastic tensor appropriate for simple shear of Ppv at the base of the mantle derived from the Walker *et al.* (2011) study for the three slip planes: (100), (010) and (001). We have used this approach in previous modelling work as well; see Creasy *et al.* (2017) for details. The second example of a geodynamically based elasticity scenario comes from a recent study by Tommasi *et al.* (2018), who carried out 2-D modelling of a (generic) upwelling at the base of the mantle, and implemented a model of texturing in a polyphase aggregate of 70 per cent Ppv and 30 per cent Fp. For this test, we use elastic tensors derived from a part of the model that is dominated by horizontal flow towards the upwelling, as well as from a part of the model dominated by vertical upwelling flow (models from upwelling streamlines at (X,Y) = (–300, 31.5) km and (X,Y) = (–27.02, 274.78) km from supplementary tables in Tommasi *et al.* 2018).

To compare with the predictions of our models, we use a subset of our measurements sampling the region directly surrounding the base of the Iceland plume. We focus on modelling our ScS splitting measurements, given that the spatial pattern in fast direction geometry is very clear; we do not include the SKS–SKKS paths in our modelling, as the geographic patterns are less clear-cut and the interpretation of the measurements in terms of D$''$-associated splitting is less straightforward. We include in our modelling the three ScS paths, assuming path R1 (Fig. 5) samples nearly vertical flow (with $V_{SV} > V_{SH}$) within the base of the plume itself, while paths R2 and R3 sample horizontal flow (with $V_{SH} > V_{SV}$) outside of it. We focus on modelling the average ScS fast splitting directions, rather than the delay times, for two reasons. First, a correct prediction of the strength of anisotropy requires accurate modelling of how anisotropy accumulates through a flow field (which, in turn, requires detailed knowledge of the relative strength of slip systems in dislocation glide, which are poorly known for the pressures and temperatures associated with the lowermost mantle). Secondly, because there is a direct tradeoff between the strength of anisotropy and the thickness of the anisotropic layer, which might not be uniform throughout our study region, it is difficult to interpret differences in shear wave splitting delay times directly in terms of differences in anisotropy strength. For these reasons, our modelling approach focuses on matching the fast splitting directions, rather than the delay times. In our modelling, we assume the mechanism for anisotropy inside and outside of the Iceland low-velocity region are the same, but the gradient in shear wave splitting behavior is due to a change in direction of flow. This would be consistent either with a scenario of pre-existing fabric due to horizontal flow outside of the plume being overprinted due to ongoing deformation in the dislocation creep regime in a vertical upwelling geometry or with a scenario of the preexisting fabric simply being rotated into a vertical geometry by the flow field. Of course, other scenarios are possible, and could be tested with future work; it is possible that a transition in anisotropy mechanism, or in dominant deformation mechanism, could also be present in the lowermost mantle beneath Iceland.

4.3.2 Modelling results

Fig. 7 illustrates our modelling approach and selected results; here, we plot all models that successfully reproduce the ScS observations, while the unsuccessful model predictions are shown in the Supplementary Information (Fig. S19). For each anisotropy scenario tested (Figs 7 and S19), we show the predicted ScS splitting behavior for both the horizontal flow region outside Iceland and for the cylindrically symmetric upwelling directly beneath it. We computed predicted fast directions for each ScS path by solving the Christoffel equation for propagation in the appropriate direction, using the MSAT toolkit (Walker & Wookey 2012), assuming horizontal propagation along the CMB. To display the horizontal flow predictions, we use a plotting convention where the splitting predictions are shown with respect to the direction of horizontal mantle flow (shear direction), assuming flow is directed towards the centre of the low-velocity region directly beneath Iceland. For vertical flow predictions, the anisotropy is symmetric with respect to the vertical symmetry axis, making the choice of north and west directions arbitrary. On each splitting prediction diagram, we highlight the predicted splitting fast direction for the actual ScS raypaths in our data set. We evaluate each model against the ScS fast directions comparing the predicted and observed fast directions, discarding those models differing by more than 20°.

Several of the cases we tested did not successfully predict the observations (Fig. S19). For Ppv, we found that both of the candidate slip systems could reproduce one of the observed ScS splitting directions (either inside or outside the Iceland region), but not both flow regimes at the same time (Fig. S19). For the [100](010) dominant slip system for Ppv, the horizontal flow case cannot reproduce the ScS splitting from path R2 (Fig. 5) because Ppv predicts weak splitting for this particular raypath direction. For the [010](001) dominant slip system, path R2 (horizontal flow) of ScS splitting could be reproduced, but not the vertical case (path R1 in Fig. 5), since the predicted fast direction is $V_{SH} > V_{SV}$ and predicted splitting is weak for a horizontally propagating ScS wave. We found that Fp, deforming on the slip system 1/2<110>100, is also an unacceptable fit to the data (Fig. S19). While this slip system could reproduce path R1 ScS (vertical flow) results, the horizontal flow case cannot reproduce path R2 ScS results. The horizontal Fp predicts $V_{SV} > V_{SH}$, which was not observed for path R1 in Fig. 5. For Br with a dominant [100](010) slip system, the model does not make predictions that are consistent with the observed ScS fast splitting directions; specifically, it predicts fast polarization directions for ScS roughly 90° away from observations for both flow regions. We found oblate SPO could reproduce path R2 ScS results (horizontal), but not path R1 ScS results (vertical), as little or no splitting is predicted for ScS in the vertical flow regime for oblate SPO. For the LPO models of Ppv from Walker *et al.* (2011) models, they all predict weak anisotropy or tilted transverse isotropy for the horizontal flow case (path #2 from Fig. 7). Since these models could not predict the ScS measurements for path R2, they were discarded as possibilities.

In contrast to these unsuccessful cases, our modelling shows that several other plausible scenarios can successfully reproduce our ScS splitting observations. We show all plausible models in Fig. 7. Tubule SPO provides an appropriate fit to the data for both the horizontal and vertical flow cases (regions both inside and outside the low-velocity region beneath Iceland), under the assumption the long axis of the inclusions is aligned with the shear direction of finite strain. While tubule SPO can reproduce the ScS results for the fast polarization directions, a 5 per cent volume fraction of inclusions only predicts $2-3$ s of delay time. Our observations indicate somewhat higher delay times, which would suggest a higher volume fraction of melt. We found that single crystal bridgmanite with a dominant [001] or [010] slip direction on the (100) slip plane also reproduces our observations (Fig. 7). LPO of ferropericlase also provides a fit to the ScS data when the 1/2<110>110 slip system is invoked (Fig. 7). Tommasi *et al.* (2018) models for an upwelling streamline also fits the change in ScS anisotropy, where $V_{SH} > V_{SV}$ is present at the base of an upwelling region. However, at the top of plume, fast directions vary with azimuth and are very close to $V_{SV} > V_{SH}$, similar to the ScS observations in path #1.

This modelling exercise does not uniquely constrain an anisotropic geometry or flow scenario at the base of the mantle beneath Iceland; however, it does provide a test for flow scenario (a localized, cylindrically symmetric upwelling) suggested by the work of He *et al.* (2015) and Yuan & Romanowicz (2017). Our modelling results show that our ScS observations are indeed consistent with this flow scenario for the four cases shown in Fig. 7: tubule SPO, bridgmanite (dominant [001] or [010] slip direction on the (100) slip plane), ferropericlase (slip system of 1/2<110>110), and the combined Ppv + Fp model of Tommasi *et al.* (2018). Our modelling further suggests that a Ppv, along with oblate SPO, and certain slip systems of Br and Fp, do not represent plausible anisotropy mechanisms beneath Iceland when combined with the flow geometry tested in this study.

5 CONCLUSION

In this study, we combined differential SKS–SKKS and S–ScS shear wave splitting from multiple azimuths to examine D″ anisotropy beneath Iceland and investigate the possible pattern of mantle flow. Our data set of differential S–ScS splitting measurements and SKS–SKKS splitting intensity discrepancies strongly suggests presence of lowermost mantle anisotropy beneath Iceland, with the the anisotropic properties of D″ directly beneath Iceland differing significantly from those of the surrounding mantle. In particular, we observe a dramatic rotation in ScS fast splitting directions for paths sampling directly beneath Iceland compared to paths sampling outside of it. We also observe a number of discrepant SKS–SKKS measurements for pairs sampling D″ surrounding Iceland; while there are only weak correlations between the location of SKS–SKKS splitting discrepancies and geographic features such as the low-velocity zone, these measurements provide complementary evidence for the presence of lowermost mantle anisotropy beneath the region. Our data suggest a localized change in either anisotropy mechanism or flow direction (or perhaps both) directly beneath Iceland, colocated with low shear velocities in tomographic models and with the presence of ULVZ material inferred from waveform modelling studies. We carry out simple forward modelling to test whether our observations are consistent with a simple flow scenario that invokes cylindrically symmetric upwelling flow at the base of the mantle within the low-velocity region and horizontal mantle flow outside of it. Our modelling results show this flow geometry is consistent with our observations if anisotropy is due to SPO of partial melt oriented in a tubule geometry, due to aligned bridgmanite with a [001] or [010] dominant slip direction on the (100) plane, due to alignment of ferropericlase, or due to texturing of a Ppv + Fp aggregate in the presence of an upwelling flow. While our observations do not uniquely constrain the geometry of mantle flow beneath Iceland, they strongly suggest a lateral transition in anisotropic geometry, and are consistent with the general idea of upwelling flow at the base of the mantle directly beneath Iceland. Our anisotropy measurements therefore generally support the notion that Iceland hotspot volcanism is sourced by a deep mantle plume and thus connected to processes in the lowermost mantle just above the CMB. We caution, however, that the interpretation of our splitting observations is non-unique, and that our interpretations based on a ray theoretical framework must be validated by future finite-frequency waveform modelling for more realistic anisotropy geometries at the base of the mantle, including the consideration of more realistic geodynamic models for thermochemical plume flow.

ACKNOWLEDGEMENTS

J.W. was supported by a scholarship from the Studienstiftung des deutschen Volkes, M.D.L. by the U.S. National Science Foundation (NSF) via grant EAR-1547499 and N.C. via an NSF Graduate Research Fellowship (grant DGE-1122492). C.T. and A.P. received funding from the European Union Horizon 2020 research and innovation program under the Marie Sklodowska-Curie grant agreement No 642029 - ITN CREEP. Some figures were prepared using the Generic Mapping Tools (Wessel & Smith 1998). We used data from the Global Seismographic Network, Askja 2007 temporary array, the Danish Seismological Network, GEOSCOPE, NORSAR, Yellowknife Array, POLARIS array and Great Britain Seismograph Network. Except for YKA and POLARIS, all data were downloaded from the Data Management Center (DMC) of the Incorporated Research Institutions for Seismology (IRIS). YKA and POLARIS data was made available by Natural Resources Canada. We are grateful to Andy Nowacki for permission to use Fig. 2(a), which was reprinted from Nature with permission from MacMillan Publishers Ltd. We are thankful to Yumei He for providing us further information about her previous work. We thank anonymous reviewers of this paper, as well as reviewers of an earlier version, for insightful comments that helped us to improve the work.

REFERENCES

Barruol, G., Paul, G.S. & Vauchez, A., 1997. Seismic anisotropy in the eastern United States: deep structure of a complex continental plate, *J. geophys. Res.,* **102,** 8329–8348.

Benoit, M.H., Long, M.D. & King, S., 2013. Anomalously thin transition zone and apparently isotropic upper mantle beneath Bermuda: evidence for upwelling beneath Bermuda, *Geochem. Geophys. Geosyst.,* **14,** 4282–4291.

Berryman, J.G., 2000. Seismic velocity decrement ratios for regions of partial melt in the lower mantle, *Geophys. Res. Lett.,* **27,** 421–424.

Bostock, M.G. & Cassidy, J.F., 1995. Variations in SKS splitting across western Canada, *Geophys. Res. Lett.,* **22**(1), 5–8.

Chen, X., Li, Y. & Levin, V., 2018. Shear wave splitting beneath eastern North American continent: evidence for a multilayered and laterally variable anisotropic structure, *Geochem. Geophys. Geosyst.,* **19,** 2857–2871.

Chevrot, S., 2000. Multichannel analysis of shear wave splitting, *J. geophys. Res.: Solid Earth,* **105,** 21 579–21 590.

Cobden, L., Thomas, C. & Trampert, J., 2015. Seismic detection of post-perovskite inside the Earth, in *The Earth's Heterogeneous Mantle: A Geophysical, Geodynamical, and Geochemical Perspective,* pp. 391–440, eds Khan, A. & Deschamps, F., Springer.

Creasy, N., Long, M.D. & Ford, H.A., 2017. Deformation in the lowermost mantle beneath Australia from observations and models of seismic anisotropy, *J. geophys. Res.: Solid Earth,* **122,** 5243–5267.

Crotwell, P., Owens, T.J. & Ritsema, J., 1999. The TauP Toolkit: flexible seismic travel-time and raypath utilities, *Seismol. Res. Lett.,* **70**(2), 154–160.

Deng, J., Long, M.D., Creasy, N., Wagner, L., Beck, S., Zandt, G., Tavera, H. & Minaya, E., 2017. Lowermost mantle anisotropy near the eastern edge of the Pacific LLSVP: constraints from SKS–SKKS splitting intensity measurements, *J. geophys. Int.,* **210,** 774–786.

Eaton, D., Frederiksen, A. & Miong, S.-K., 2004. Shear-wave splitting observations in the lower Great Lakes region: evidence for regional anisotropic domains and keel-modified asthenospheric flow, *Geophys. Res. Lett.,* **31**(7), doi:10.1029/2004GL019438.

Foley, B.J. & Long, M.D., 2011. Upper and mid–mantle anisotropy beneath the Tonga slab, *Geophys. Res. Lett.,* **38**(2), doi:10.1029/2010GL046021.

Ford, H.A., Long, M.D., He, X. & Lynner, C., 2015. Lowermost mantle flow at the eastern edge of the African Large Low Shear Velocity Province, *Earth planet. Sci. Lett.,* **420,** 12–22.

Foulger, G. & Anderson, D., 2005. A cool model for the Iceland hotspot, *J. Volc. Geotherm. Res.,* **141,** 1–22.

French, S. & Romanowicz, B., 2015. Broad plumes rooted at the base of the Earth's mantle beneath major hotspots, *Nature,* **525,** 95–99.

Girard, J., Chen, J. & Raterron, P., 2012. Deformation of periclase single crystals at high pressure and temperature: quantification of the effect of pressure on slip-system activities, *J. Appl. Phys.,* **111,** 112607.

Goryaeva, A., Carrez, P. & Cordier, P., 2016. Low viscosity and high attenuation in MgSiO3 post-perovskite inferred from atomic-scale calculations, *Scient. Rep.,* **6,** 34771.

Gouriet, K., Carrez, P. & Cordier, P., 2014. Atomic core structure and mobility of [100](010) and [010](100) dislocations in $MgSiO_3$ perovskite, *Acta Mater.,* **79,** 1–17.

Gudmundsson, A., 2000. Dynamics of volcanic systems in Iceland: example of tectonism and volcanism at juxtaposed hot spot and mid-ocean ridge systems, *Ann. Rev. Earth planet. Sci.,* **28,** 107–140.

He, Y., Wen, L., Capdeville, Y. & Zhao, L., 2015. Seismic evidence for an Iceland thermo-chemical plume in the Earth's lowermost mantle, *Earth planet. Sci. Lett.,* **417,** 19–27.

Hernlund, J. & Jellinek, M., 2010. Dynamics and structure of a stirred partially molten ultralow-velocity zone, *Earth planet. Sci. Lett.,* **296,** 1–8.

Hernlund, J. & McNamara, A., 2015. The core-mantle boundary region, *Treat. Geophys.,* **7,** 461–519.

Hier-Majumder, S. & Drombosky, T.W., 2016. Coupled flow and anisotropy in the ultralow velocity zones, *Earth planet. Sci. Lett.,* **450,** 274–282.

Hirose, K., 2006. Postperovskite phase transition and its geophysical implications, *Rev. Geophys.,* **44**(3), doi:10.1029/2005RG000186.

Immoor, J. *et al.* 2018. Evidence for 100< 011> slip in ferropericlase in Earth's lower mantle from high-pressure/high-temperature experiments, *Earth planet. Sci. Lett.,* **489,** 251–257.

Karato, S.-I., 1998. Seismic anisotropy in the deep mantle, boundary layers and the geometry of mantle convection, *Pure appl. geophys.,* **151**(2–4), 565–587.

Karato, S.-I., Jung, H., Katayama, I. & Skemer, P., 2008. Geodynamic significance of seismic anisotropy of the upper mantle: new insights from laboratory studies, *Ann. Rev. Earth planet. Sci.,* **36,** 59–95.

Karki, B.B., Wentzcovitch, R.M., de Gironcoli, S. & Baroni, S., 1999. First-principles determination of elastic anisotropy and wave velocities of MgO at lower mantle conditions, *Science,* **286,** 1705–1707.

Kawai, K. & Geller, R.J., 2010. Waveform inversion for localized seismic structure and an application to D structure beneath the Pacific, *J. geophys. Res.: Solid Earth,* **115**(B1), doi:10.1029/2009JB006503.

Kendall, J.-M. & Silver, P., 1998. Investigating causes of D″ anisotropy, *The Core-Mantle Boundary Region, Geodynamic Series,* Vol. **28,** pp. 97–118, eds Gurnis M., Wysession M. E., Knittle E., & Buffett B. A., American Geophysical Union.

Kennett, B.L.N. & Engdahl, E.R., 1991. Traveltimes for global earthquake location and phase identification, *J. geophys. Int.,* **105,** 429–465.

Kraych, A., Carrez, P. & Cordier, P., 2016. On dislocation glide in $MgSiO_3$ bridgmanite at high-pressure and high-temperature, *Earth planet. Sci. Lett.,* **452,** 60–68.

Lee, K.K.M., O'Neill, B., Wendy, R.P., Shim, S.-H., Benedetti, L. & Jeanloz, R., 2004. Equations of state of the high-pressure phases of a natural peridotite and implications for the Earth's lower mantle, *Earth planet. Sci. Lett.,* **223,** 381–393.

Lin, S.-C. & van Keken, P.E., 2006. Dynamics of thermochemical plumes: 2. Complexity of plume structures and its implications for mapping mantle plumes, *Geochem. Geophys. Geosyst.,* **7**(3), doi:10.1029/2005GC001072.

Lin, Y.-P., Zhao, L. & Hung, S.-H., 2014. Full-wave effects on shear wave splitting, *Geophys. Res. Lett.,* **41,** 799–804.

Long, M., 2009. Complex anisotropy in D beneath the eastern Pacific from SKS–SKKS splitting discrepancies, *Earth planet. Sci. Lett.,* **283,** 181–189.

Long, M.D. & Becker, T., 2010. Mantle dynamics and seismic anisotropy, *Earth planet. Sci. Lett.,* **297,** 341–354.

Long, M.D. & Lynner, C., 2015. Seismic anisotropy in the lowermost mantle near the Perm Anomaly, *Geophys. Res. Lett.,* **42,** 7073–7080.

Long, M.D. & Silver, P.G., 2009. Shear wave splitting and mantle anisotropy: measurements, interpretations, and new directions, *Surv. Geophys.,* **30,** 407–461.

Lynner, C. & Long, M., 2012. Evaluating contributions to SK(K)S splitting from lower mantle anisotropy: a case study from station DBIC, Cote D'Ivoire, *Bull. seism. Soc. Am.,* **102,** 1030–1040.

Lynner, C. & Long, M.D., 2014. Lowermost mantle anisotropy and deformation along the boundary of the African LLSVP, *Geophys. Res. Lett.,* **41,** 3447–3454.

Miyagi, L. & Wenk, H.-R., 2016. Texture development and slip systems in bridgmanite and bridgmanite+ferropericlase aggregates, *Phys. Chem. Miner.,* **43,** 597–613.

Miyagi, L., Kanitpanyacharoen, W., Kaercher, P., Lee, K.K.M. & Wenk, H.-R., 2010. Slip systems in $MgSiO_3$ post-perovskite: implications for D" anisotropy, *Science,* **329,** 1639–1641.

Montagner, J.-P. & Anderson, D.L., 1989. Petrological constraints on seismic anisotropy, *Phys. Earth planet. Inter.,* **54,** 82–105.

Murakami, M., Hirose, K., Kawamura, K., Sata, N. & Ohishi, Y., 2004. Post-perovskite phase transition in $MgSiO_3$, *Science,* **304,** 855–858.

Nowacki, A. & Wookey, J., 2016. The limits of ray theory when measuring shear wave splitting in the lowermost mantle with ScS waves, *J. geophys. Int.,* **207,** 1573–1583.

Nowacki, A., Wookey, J. & Kendall, J.-M., 2010. Deformation of the lowermost mantle from seismic anisotropy., *Nature,* **467,** 1091–1094.

Nowacki, A., Wookey, J. & Kendall, J.-M., 2011. New advances in using seismic anisotropy, mineral physics and geodynamics to understand deformation in the lowermost mantle, *J. Geodyn.,* **52,** 205–228.

Panning, M. & Romanowicz, B., 2006. A three-dimensional radially anisotropic model of shear velocity in the whole mantle, *J. geophys. Int.,* **167,** 361–379.

Parisi, L., Ferreira, A.M.G. & Ritsema, J., 2018. Apparent splitting of S waves propagating through an isotropic lowermost mantle, *J. geophys. Res.: Solid Earth,* **123,** 3909–3922.

Rao, P.B., Kumar, M. & Singh, A., 2017. Anisotropy in the lowermost mantle beneath the Indian Ocean Geoid Low from ScS splitting measurements, *Geochem. Geophys. Geosyst.,* **18,** 13 385–13 393.

Restivo, A. & Helffrich, G., 2006. Core-mantle boundary structure investigated using SKS and SKKS polarization anomalies, *J. geophys. Int.,* **165,** 288–302.

Samuel, H. & Bercovici, D., 2006. Oscillating and stagnating plumes in the Earth's lower mantle, *Earth planet. Sci. Lett.,* **248,** 90–105.

Silver, P.G. & Chan, W.W., 1991. Shear wave splitting and subcontinental mantle deformation, *J. geophys. Res.: Solid Earth,* **96,** 16 429–16 454.

Simmons, N.A., Forte, A.M., Boschi, L. & Grand, S.P., 2010. GyPSuM: a joint tomographic model of mantle density and seismic wave speeds, *J. geophys. Res.: Solid Earth,* **115,** B12310.

Stackhouse, S., Brodholt, J.P. & Price, G.D., 2006. Elastic anisotropy of $FeSiO_3$ end-members of the perovskite and post-perovskite phases, *Geophys. Res. Lett.,* **33**(1), doi:10.1029/2005GL023887.

Tandon, G.P. & Weng, G.J., 1984. The effect of aspect ratio of inclusions on the elastic properties of unidirectionally aligned composites, *Polym. Compos.,* **5,** 327–333.

Tommasi, A., Goryaeva, A., Carrez, P., Cordier, P. & Mainprice, D., 2018. Deformation, crystal preferred orientations, and seismic anisotropy in the Earth's D" layer, *Earth planet. Sci. Lett.,* **492,** 35–46.

Walker, A. & Wookey, J., 2012. MSAT—a new toolkit for the analysis of elastic and seismic anisotropy, *Comput. Geosci.,* **49,** 81–90.

Walker, A.M., Forte, A.M., Wookey, J., Nowacki, A. & Kendall, J.-M., 2011. Elastic anisotropy of D″ predicted from global models of mantle flow, *Geochem. Geophys. Geosyst.,* **12**(10), doi:10.1029/2011GC003732.

Wang, Y. & Wen, L., 2004. Mapping the geometry and geographic distribution of a very low velocity province at the base of the Earth's mantle, *J. geophys. Res.: Solid Earth,* **109**(B10), doi:10.1029/2003JB002674.

Wessel, P. & Smith, W.H.F., 1998. New, improved version of generic mapping tools released, *EOS, Trans. Am. Geophys. Un.,* **79,** 579–579.

Williams, Q. & Garnero, E.J., 1996. Seismic evidence for partial melt at the base of Earth's mantle, *Science,* **273**(5281), 1528–1530.

Wolfe, C.J., Bjarnason, I., VanDecar, J. & Sean, C.S., 1997. Seismic structure of the Iceland mantle plume, *Nature,* **385,** 245–247.

Wookey, J., Kendall, J.-M. & Rümpker, G., 2005a. Lowermost mantle anisotropy beneath the north Pacific from differential S–ScS splitting, *J. geophys. Int.,* **161,** 829–838.

Wookey, J., Stackhouse, S., Kendall, J.-M., Brodholt, J. & Price, G., 2005b. Efficacy of the post-perovskite phase as an explanation for lowermost-mantle seismic properties, *Nature,* **438,** 1004–1007.

Wüstefeld, A., Bokelmann, G., Zaroli, C. & Barruol, G., 2008. Splitlab: a shear-wave splitting environment in MATLAB, *Comput. Geosci.,* **34,** 515–528.

Wüstefeld, A., Al-Harrasi, O., Verdon, J.P., Wookey, J. & Kendall, J.M., 2010. A strategy for automated analysis of passive microseismic data to image seismic anisotropy and fracture characteristics, *Geophys. Prospect.,* **58**(5), 755–773.

Yamazaki, D. & Karato, S.-I., 2001. High-pressure rotational deformation apparatus to 15 GPa, *Rev. Scient. Instrum.,* **72,** 4207–4211.

Yang, B., Liu, Y., Dahm, H., Liu, K. & Gao, S., 2017. Seismic azimuthal anisotropy beneath the eastern United States and its geodynamic implications, *Geophys. Res. Lett.,* **44**(6), 2670–2678.

Yu, S. & Garnero, E.J., 2018. Ultralow velocity zone locations: a global assessment, *Geochem. Geophys. Geosyst.,* **19**(2), 396–414.

Yuan, K. & Romanowicz, B., 2017. Seismic evidence for partial melting at the root of major hot spot plumes, *Science,* **357,** 393–397.

SUPPORTING INFORMATION

Supplementary data are available at *GJI* online.

Supplementary_Material_revised.pdf

Please note: Oxford University Press is not responsible for the content or functionality of any supporting materials supplied by the authors. Any queries (other than missing material) should be directed to the corresponding author for the paper.